J Mater Sci: Mater Electron (2025) 36:1558

Photoelectrochemical engineering of $Cu_{1.94}S$ nanoparticles towards a low temperature atmospheric synthesis method

Seyed Ali Hosseini Moradi[1,*] and Farzad Namvar[2]

[1] *Department of Physics, Khatam Al-Anbia Air Defense University (PBUH), P.O. Box: 178183513, Tehran, Iran*
[2] *College of Pharmacy, Al-Hadba University, Mosul, Iraq*

Received: 24 April 2025
Accepted: 20 August 2025

ABSTRACT

$Cu_{2-x}S$ photocatalysts have demonstrated robust performance in various applications, including pollutant degradation, sensors, and chemicals synthesis under visible light, owing to their unique properties. Compared to noble-metal-based photocatalysts, the low cost of copper and sulfur makes $Cu_{2-x}S$ photocatalysts attractive for industrial use. However, developing a simple and scalable synthesis method remains a challenge. In this study, a low-temperature, atmospheric-pressure route was introduced to synthesize $Cu_{1.94}S$ nanoparticles. XRD analysis confirmed that using Tween 20 as a capping agent at 60 °C yields $Cu_{1.94}S$ nanoparticles, whereas using Triton X-100 under the same conditions results in CuS. FESEM and TEM images revealed that the $Cu_{1.94}S$ nanoparticles are spherical with a strong tendency to aggregate. UV–Vis and photoluminescence analyses showed that the band gap of $Cu_{1.94}S$ could be tuned through this method, reaching a value of 1.66 eV. Furthermore, linear sweep voltammetry and electrochemical impedance spectroscopy indicated a significant enhancement in the electrochemical performance of $Cu_{1.94}S$-coated electrodes compared to bare titanium electrodes.

1 Introduction

The expansion of industries and the increase in population worldwide have led to increased governmental attention to the use of renewable energy sources. One of the most important types of renewable energy is solar energy, which has gained significant interest for applications in solar cells [1], water purification systems [2–4], and desalination plants [5]. One of the prerequisites for the utilization of solar energy in these systems is the design of semiconductors with improved optical properties. Despite the design and introduction of various semiconductors such as TiO_2 [6], WO_3 [7], SnO_2/ZnO [8], V_2O_5/TiO_2 [9] and others, extensive research is still ongoing to develop new materials with better performance and cheaper raw materials. Recent studies on MnTiO2 and SnO2 have indicated that the high surface area, robust chemical stability, and efficient interactions with light and biological systems make them ideal candidates for

Address correspondence to E-mail: physicplasma2011@gmail.com
E-mail Addresses: Namvar.fa@gmail.com

https://doi.org/10.1007/s10854-025-15637-7
Published online: 29 August 2025

applications such as antibacterial agents, antioxidant platforms, and photocatalysts [10, 11]. Complementing traditional synthesis approaches, recent efforts have turned toward environmentally benign production strategies—particularly those utilizing plant-based extracts—which offer a greener and more sustainable pathway. This shift underscores the growing emphasis on eco-conscious innovation in nanomaterial research and the emerging role of metal oxide nanoparticles in addressing contemporary scientific challenges [12–14]. At the nanoscale, metal oxides demonstrate tunable physical and chemical characteristics, with morphology, surface defects, and particle size playing key roles in boosting reactive oxygen species generation—essential for antibacterial and antioxidant effectiveness. Their inherent biocompatibility and minimal toxicity further support their integration into biomedical and environmental technologies, as confirmed through various characterization techniques [15, 16]. Recent advances in nanoscale engineering have revealed how modifications at the atomic level can significantly alter surface energy and electronic properties, thereby enabling stronger biological interactions and improved therapeutic efficacy [17–20]. Moreover, emerging studies on transition metal chalcogenide (TMC) nanostructures have emphasized their potential in photoelectrochemical applications. Their ability to absorb light efficiently and support rapid charge transfer renders them suitable for solar-driven water splitting and related energy technologies. The performance of these systems is closely tied to nanoscale features, which continue to be optimized to unlock their full potential. Incorporating recent developments in this area provides a more robust foundation for current investigations and reinforces the significance of ongoing research [21–24].

Transition metal sulfides (e.g. MoS_2 [25]) have exhibited unique properties. One material that has shown attractive optoelectronic properties in addition to being non-toxic and inexpensive is copper sulfide [26]. Copper sulfide is a p-type semiconductor with the general formula Cu_xS, where x can take different values. Depending on the composition and size of the nanoparticles, Cu_xS has a band gap in the visible to ultraviolet light range [27, 28]. For this reason, copper sulfide nanoparticles have been designed for various applications such as water purification [29, 30], air purification [31], hydrogen evolution reaction (HER) [32], photocatalytic reactions of hydrocarbons [33], solar cells [34], and desalination [35]. Another feature of copper sulfides in the form of $Cu_{2-x}S$ ($0 \le x \le 0.25$) is their tunable thermoelectric properties, which makes them attractive for thermoelectric applications [36, 37]. Proper utilization of these materials requires a precise understanding of their stoichiometry, phase structure, and electronic properties under different operating conditions, which has not yet been fully elucidated [27, 38]. For example, Li et al. [39] investigated the effect of annealing atmosphere (pure argon or 5% hydrogen + argon) at 450 °C on the electrical conductivity and Seebeck coefficient of $Cu_{2-x}S$ nanoparticles. However, Zuo et al. [40] aimed to improve the power factor of $Cu_{2-x}S$ films by adding manganese and finding its optimum amount.

It should be noted that one of the main reasons for the attractiveness of copper sulfides is the low cost of this material for industrial applications. However, in order to achieve this goal, the production method must also be inexpensive with minimal energy consumption. Several methods have been proposed for the synthesis of $Cu_{2-x}S$ nanoparticles, most of which operate at pressures above atmospheric [40–42] and temperatures above 140 °C [31, 39]. Methods have also been developed at atmospheric pressure and temperatures below 70 °C, but due to the use of expensive raw materials such as L-cystine and L-cysteine, their industrial applicability is limited [43, 44]. Pathan et al. [45] also proposed a method using inexpensive materials at room temperature, which is suitable for the preparation of thin films of Cu_2S on glass substrates, not for Cu_2S nanoparticles. The synthesis and tuning of the optoelectronic properties of copper sulfide nanoparticles involves many complexities, which can arise not only from the different possible Cu to S stoichiometries, but also from the high mobility of Cu atoms in their crystal lattice [46].

Therefore, the aim of this work was to propose a method for the synthesis of $Cu_{2-x}S$ nanoparticles using inexpensive materials with potential for industrialization, at low temperature and atmospheric pressure. It was also decided to tune the band gap of the synthesized nanoparticles in the visible light region with the developed method, making them suitable for photocatalytic applications under sunlight along with desirable electrochemical properties. In this regard, copper sulfide nanoparticles were synthesized using two different nonionic capping agents, Tween 20 and Triton X100, at two temperatures of 25 and 60 °C using the same method. It was observed that the nanoparticles obtained are significantly different. The synthesized

nanoparticles were carefully examined by several XRD analyses. Next, the physical structure of the nanoparticles synthesized with Tween 20 at both 25 and 60 °C was investigated using FESEM images. The optical properties of the obtained $Cu_{1.94}S$ nanoparticles were investigated by UV–Vis absorption and photoluminescence analyses. Finally, the electrochemical properties of the electrodes made of $Cu_{1.94}S$ nanoparticles were investigated by means of linear sweep voltammetry (LSV) and electrochemical impedance spectroscopy (EIS) tests.

2 Experimental method

2.1 Materials

Copper sulfate pentahydrate ($CuSO_4{\cdot}5H_2O$, ACS), sodium sulfide ($Na_2S.9H_2O$ GR), cyclohexane (C_6H_{12}, ACS), Triton X100 (AR) and absolute ethanol (ACS) were purchased from Merck. Tween 20 (AR) was purchased from Sigma-Aldrich. All the chemicals were used without further purification.

2.2 *Cu_xS nanoparticles synthesis*

To synthesize copper sulfide nanoparticles, 3.47 g of copper sulfate was first dissolved in deionized water. Then, a certain amount (21, 41.5 and 83 cc) of Tween 20 was added to the prepared copper sulfate solution. Then, 75 cc of cyclohexane was added to this solution and stirred well to prepare a reverse micellar state. In a separate beaker, 10.8 g of sodium sulfide was dissolved in 45 cc of water and this solution was added dropwise to the prepared copper sulfate mixture while stirring. The prepared mixtures were maintained at two temperatures of 25 and 60 °C for 5 h with continuous stirring. The same procedure was performed using Triton X100 at concentrations equivalent to that of Tween 20. The synthesized copper sulfide nanoparticles were then separated and washed several times with distilled water and then with absolute ethanol. The temperature and amount of capping agent used to synthesize the nanoparticles are summarized in Table 1.

2.3 Nanoparticles characterization

XRD patterns of the prepared samples were obtained for phase detection using a diffractometer (PHILIPS-PW1730) operated at 40 kV and 30 mA with Cu Kα radiation (λ = 1.5406 Å). The XRD instrument had a scan rate of 3°/min with a step size of 0.05°. SEM imaging was performed using a MIRA3 FESEM apparatus to study the physical structure of the synthesized nanoparticles. To investigate the optical properties of each sample, UV–Vis absorption and photoluminescence (PL) analyses were performed using a Shimadzu UV2600 UV–Vis spectrometer and an Agilent Cary Eclipse fluorescence spectrometer, respectively.

2.4 Electrochemical tests

An AUTOLAB potentiostat was employed for electrochemical measurements on the synthesized $Cu_{1.94}S$ nanoparticles in a conventional three-electrode setup at ambient temperature. The counter electrode was a graphite rod, while an Ag/AgCl electrode served as the reference electrode. $Cu_{1.94}S$ sheets as working electrodes were prepared by mixing 3 mg of $Cu_{1.94}S$ nanoparticles with 20 µL of PVDF/NMP solution (5 wt%), which was then extruded uniformly on both sides of a clean titanium sheet. Finally, the prepared sheets were dried at 60 °C. All experiments were performed under alkaline conditions using 1 M KOH solution. LSV analysis was performed at a scan rate of 50 mV/s. EIS measurements were performed over a frequency range of 0.1 Hz to 100 kHz using an amplitude of 5 mV.

Table 1 Temperature and amount of capping agent used to synthesize nanoparticles

Parameter	Tween 20			Tween 20			Trition X100			Trition X100		
Capping agent amount (cc)	21	41.5	83	21	41.5	83	3.5	20	45	3.5	20	45
Capping agent amount (g)	23.1	45.7	91.3	23.1	45.7	91.3	3.75	21.4	48.15	3.75	21.4	48.15
Capping agent concentration at final mixture (mol/lit)	0.1	0.2	0.3	0.1	0.2	0.3	0.1	0.2	0.3	0.1	0.2	0.3
Synthesis temperature (°C)	25	25	25	60	60	60	25	25	25	60	60	60

3 Results and discussion

3.1 XRD experiments

Figure 1 shows the XRD graphs for six samples of copper sulfide nanoparticles synthesized with Tween 20 and six samples synthesized with Triton X100. As shown in Fig. 1a, at 25 °C, when the concentration of Tween 20 is 0.1 molar, the obtained nanoparticles consist mainly of $Cu_4(SO_4)(OH)_6$ with an orthorhombic crystal structure in accordance with PDF# 29-0575 [47]. When the concentration of Tween 20 is increased to 0.2 molar, the peaks corresponding to $Cu_4(SO_4)(OH)_6$ almost disappear and the crystalline structure of CuS [48] begins to form. By further increasing the Tween 20 concentration to 0.3 molar, the hexagonal crystalline structure of CuS in accordance with PDF# 29-0575 is established and the dominant peaks correspond to this material. For the XRD graphs related to the temperature of 60 °C in Fig. 1a, a notable feature is the formation of the monoclinic crystalline structure of $Cu_{1.94}S$ (PDF# 23-0959) in all three concentrations of Tween 20 (0.1, 0.2, and 0.3 molar) [40, 50]. It can also be observed that the peaks corresponding to the medium

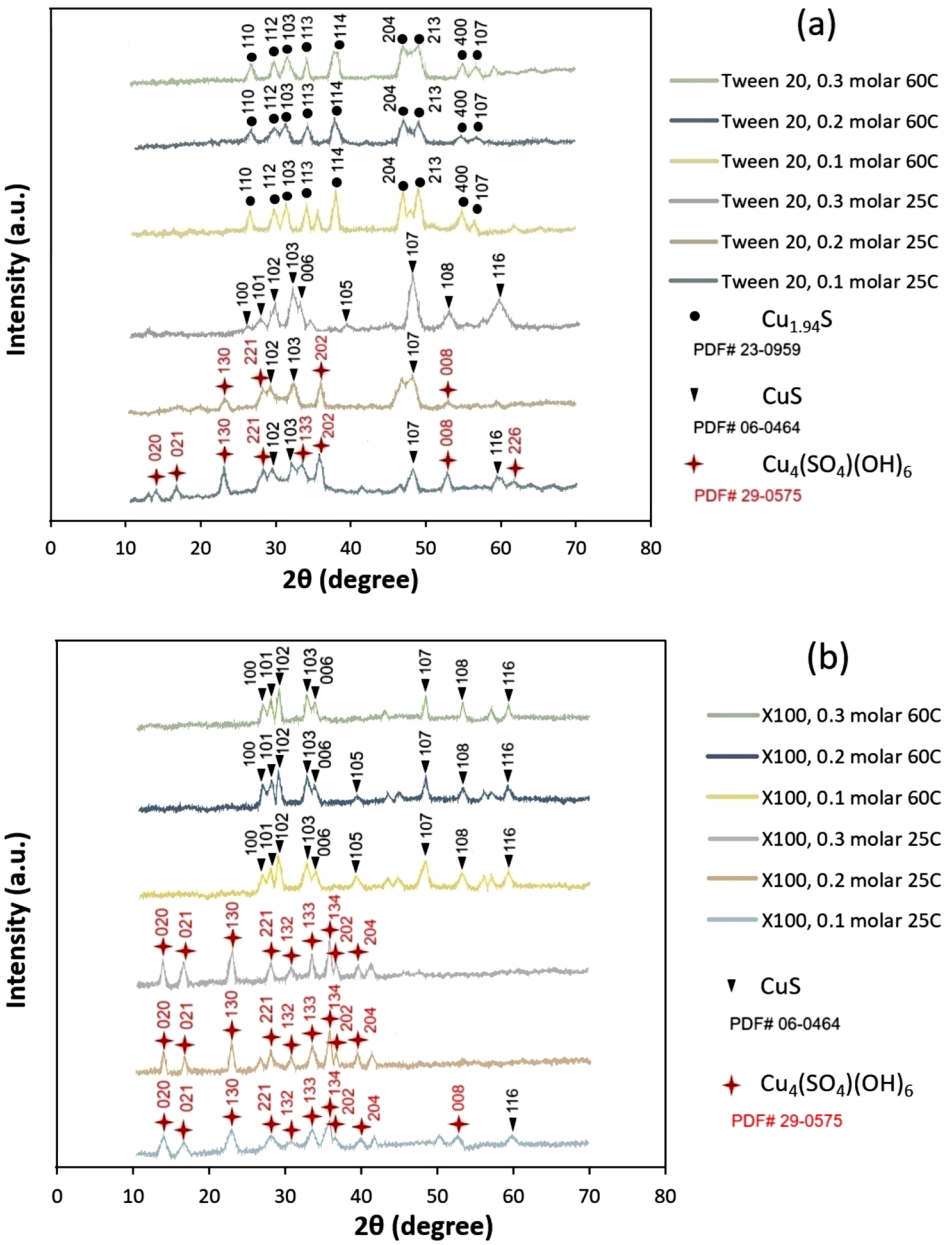

Fig. 1 XRD analysis graphs for, **a** nanoparticles synthesized with Tween 20, and, **b** nanoparticles synthesized with Triton X100

concentration of Tween 20 (0.2 molar) are weaker compared to the other two concentrations, similar to the graphs for the temperature of 25 °C. It seems that the crystals of the nanoparticles form better in the dilute mixture (0.1 molar Tween 20) and the concentrated gel (0.3 molar Tween 20) compared to the dilute gel (0.2 molar Tween 20).

Figure 1b corresponds to the XRD graphs of nanoparticles synthesized with Triton X100 at a concentration equivalent to Tween 20 and using a similar method. As observed in the graphs of Fig. 1b, at 25 °C, the orthorhombic crystal structure of $Cu_4(SO_4)(OH)_6$ (PDF# 29-0575) in the synthesized nanoparticles is clearer compared to the nanoparticles prepared with Tween 20. In addition, considering the decrease in the width of the peaks and the increase in their height, it can be concluded that with the increase in the concentration of Triton X100, the size of the $Cu_4(SO_4)(OH)_6$ crystals becomes smaller while their quantity increases. Regarding the graphs in Fig. 1b at 60 °C, the obtained nanoparticles corresponds to CuS with the hexagonal crystalline structure (PDF# 29-0575), which is in agreement with the results obtained by Nemade et al. [51]. It can also be observed that as the concentration of Triton X100 increases, the width of the peaks decreases while their heights remain constant. This indicates a decrease in the size of the CuS crystals with increasing Triton X100 concentration.

3.2 FESEM

Based on the results of the XRD analysis, the FESEM images of the nanoparticles synthesized with Tween 20 at both temperatures of 25 and 60 °C were obtained and are shown in Fig. 2. As observed at both temperatures, the nanoparticles synthesized at all three concentrations of Tween 20 show a strong tendency to form aggregates [51]. Among the nanoparticle images in Fig. 2, only the nanoparticles with a concentration of 0.1 molar Tween 20 at 25 °C (Fig. 2a) show a structure composed of dense flat sheets with some aggregates of spherical particles. Figure 3 shows the FESEM image of nanoparticles synthesized with 0.1 molar Triton X100 at 25 °C. From the similarity between Figs. 3 and 2a, it can be concluded that the dense flat sheets in Fig. 2a probably represent nanoparticles of $Cu_4(SO_4)(OH)_6$, while the small aggregates of spherical nanoparticles correspond to CuS, whose presence was confirmed in the XRD pattern of Fig. 1a. The images of CuS nanoparticles synthesized with 0.2 molar Tween 20 (Fig. 2c) and 0.3 molar Tween 20 (Fig. 2e) at 25 °C show a similar structure with a difference in particle size distribution. This difference in particle size distribution is due to the variation in the amount of capping agent, which is also observed for $Cu_{1.94}S$ nanoparticles synthesized at 60 °C (Fig. 2b, d and f). From Fig. 2b, d and f, it can be concluded that as the concentration of Tween 20 increases, the size of the nanoparticles decreases, but the aggregates become larger. In fact, as the amount of Tween 20 increases, the tendency of the nanoparticles to adhere to each other also increases, which is unfavorable for easy dispersion of the nanoparticles in a medium such as water. The mean particle sizes are given in Table 2, through a detailed analysis of the images.

In order to provide a more comprehensive perspective on the propensity of $Cu_{1.94}S$ nanoparticles to form aggregates, even when prepared with a minimal amount of Tween 20 (0.1 molar) at 60 °C, a (TEM) image is presented in Fig. 4. It is noteworthy that, given the low synthesis temperature (60 °C) of these $Cu_{1.94}S$ nanoparticles, ultrasonication was not employed for sample preparation prior to TEM imaging. The intense energy of ultrasonication has the potential to induce alterations in the chemical structure of $Cu_{1.94}S$ nanoparticles, thereby converting them into a different phase of Cu_xS.

3.3 UV–Vis and PL experiments

To evaluate the photocatalytic activity of $Cu_{1.94}S$ nanoparticles synthesized at 60 °C, UV–Vis absorption analysis (Fig. 5a) was performed for all three samples. Based on Fig. 4a, all plots have the same trend with a maximum absorption peak (λ_{maxUV} = 315 nm) in the UV region, besides an inflection point (at 498 nm) and a minimum absorption peak (λ_{minVis} = 580 nm) both in the visible region. The same trend of the UV–Vis plots, together with the identical λ_{maxUV} and λ_{minVis}, proves the same chemical composition of the samples in agreement with the XRD results. However, as the mean particle size increases, the absorption at λ_{maxUV} decreases while it increases at λ_{minVis}, indicating a red shift in the absorption of the synthesized nanoparticles.

Due to the controversial results regarding the band gap of Cu1.94S, which is direct [52] or indirect [53], the Tauc plot for both $(\alpha h\nu)^2$ (assuming direct band gap material) and $(\alpha h\nu)^{0.5}$ (assuming indirect band gap material) vs. hν was plotted (Fig. 5b and

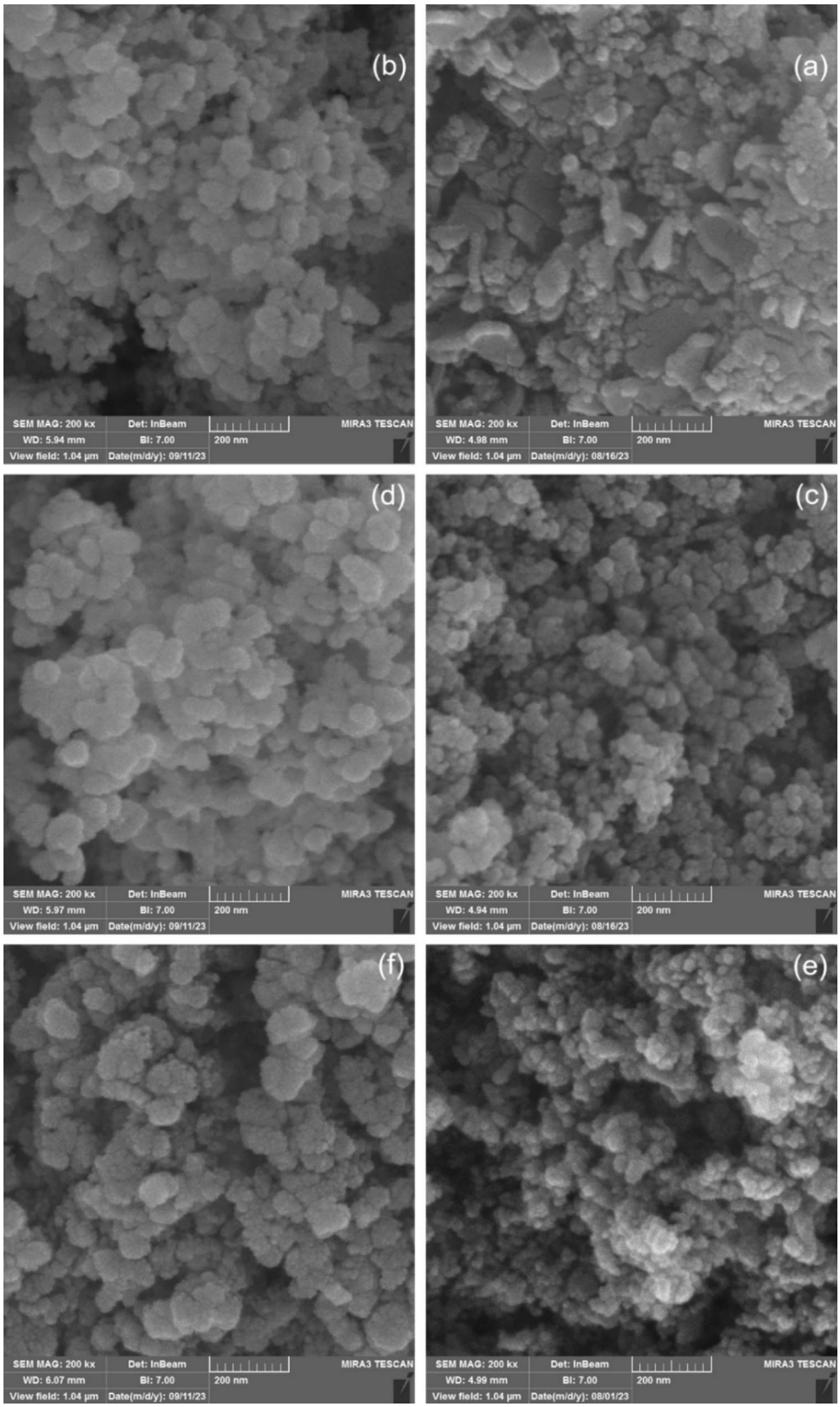

Fig. 2 FESEM imgaes of the nanoparticles synthesized with, **a** 0.1 molar Tween 20 at 25 °C, **b** 0.1 molar Tween 20 at 60 °C, **c** 0.2 molar Tween 20 at 25 °C, **d** 0.2 molar Tween 20 at 60 °C, **e** 0.3 molar Tween 20 at 25 °C, **f** 0.3 molar Tween 20 at 60 °C

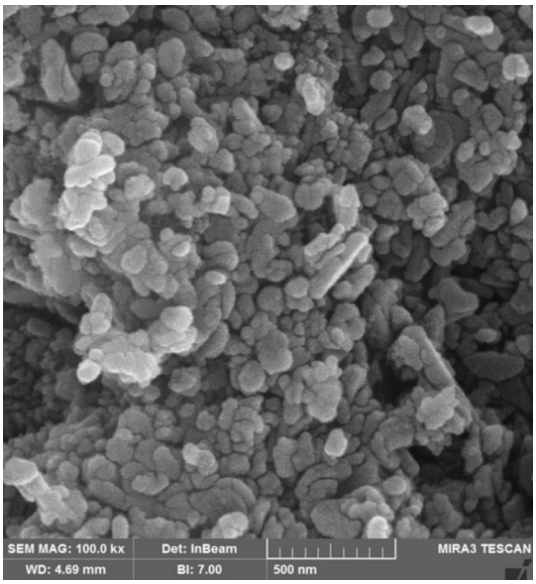

Fig. 3 FESEM image of the nanoparticles synthesized with 0.1 molar Triton X100 at 25 °C

c, respectively) for all samples using the absorption data (Fig. 5a). It is well known that for the direct band gap materials, the recombination of an electron from the conduction band and a hole from the valence band occurs at the same k-momentum, releasing a photon. But, in the case of indirect band gap materials, this recombination necessitates the release of both phonons and photons. The latter is due to different k-momentum values for the minimum of conduction band and maximum of valence band. A comparison of Fig. 5b and c reveals that the linear part of the plots is more pronounced in Fig. 5b than in Fig. 5c, indicating $Cu_{1.94}S$ is a direct bandgap material. As illustrated in Fig. 5b, the nanoparticles synthesized with 0.1, 0.2, and 0.3 molar Tween 20 exhibited direct band gaps of 1.66, 1.77, and 1.9 eV, respectively, as the linear part of the plots were extended to the x-axes. Accordingly, the band gap of the obtained nanoparticles falls in the wavelength range of 650 to 750 nm, confirming their activity in the visible light range. It is worth noting that, based on the hyperbolic band model [54], the band gap increases as the size of the nanoparticles decreases. In addition, compared with 2.15 eV as the band gap for $Cu_{1.94}S$ nanoparticles with an average size of 7 nm reported by Zhu et al. [52], it was shown that the band gap of $Cu_{1.94}S$ nanoparticles was successfully reduced using a simpler preparation method.

To further investigate and validate the obtained band gap values of $Cu_{1.94}S$ nanoparticles, PL analysis was performed on all three samples. In this experiment, an excitation wavelength of 400 nm was chosen to ensure a significant distance from the calculated band gap values obtained by the UV–Vis absorption method. It is known that the farther the excitation wavelength is from the actual band gap wavelength, the shorter the peak height corresponding to the band gap should be in the PL analysis. According to the PL analysis graphs shown in Fig. 5, it can be observed that the band gap of the samples has a small FWHM (full width at half maximum) and a high peak at a wavelength of 797 nm, corresponding to 1.56 eV. Since the calculated band gap in this

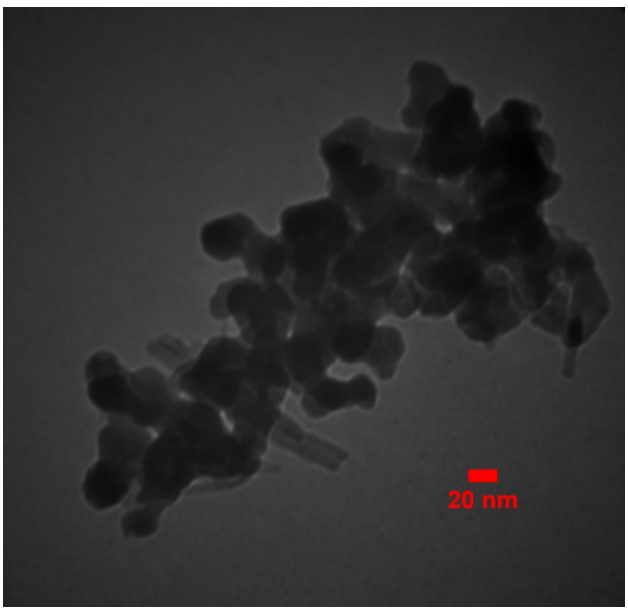

Fig. 4 TEM image of the $Cu_{1.94}S$ nanoparticles synthesized with 0.1 molar Tween 20 at 60 °C

Table 2 Mean particle size of the nanoparticles synthesized with Tween 20

Parameter	Tween 20			Tween 20		
Capping agent concentration (mol/lit)	0.1	0.2	0.3	0.1	0.2	0.3
Synthesis temperature (°C)	25	25	25	60	60	60
Mean particle size (nm)	–	35	30	45	40	35

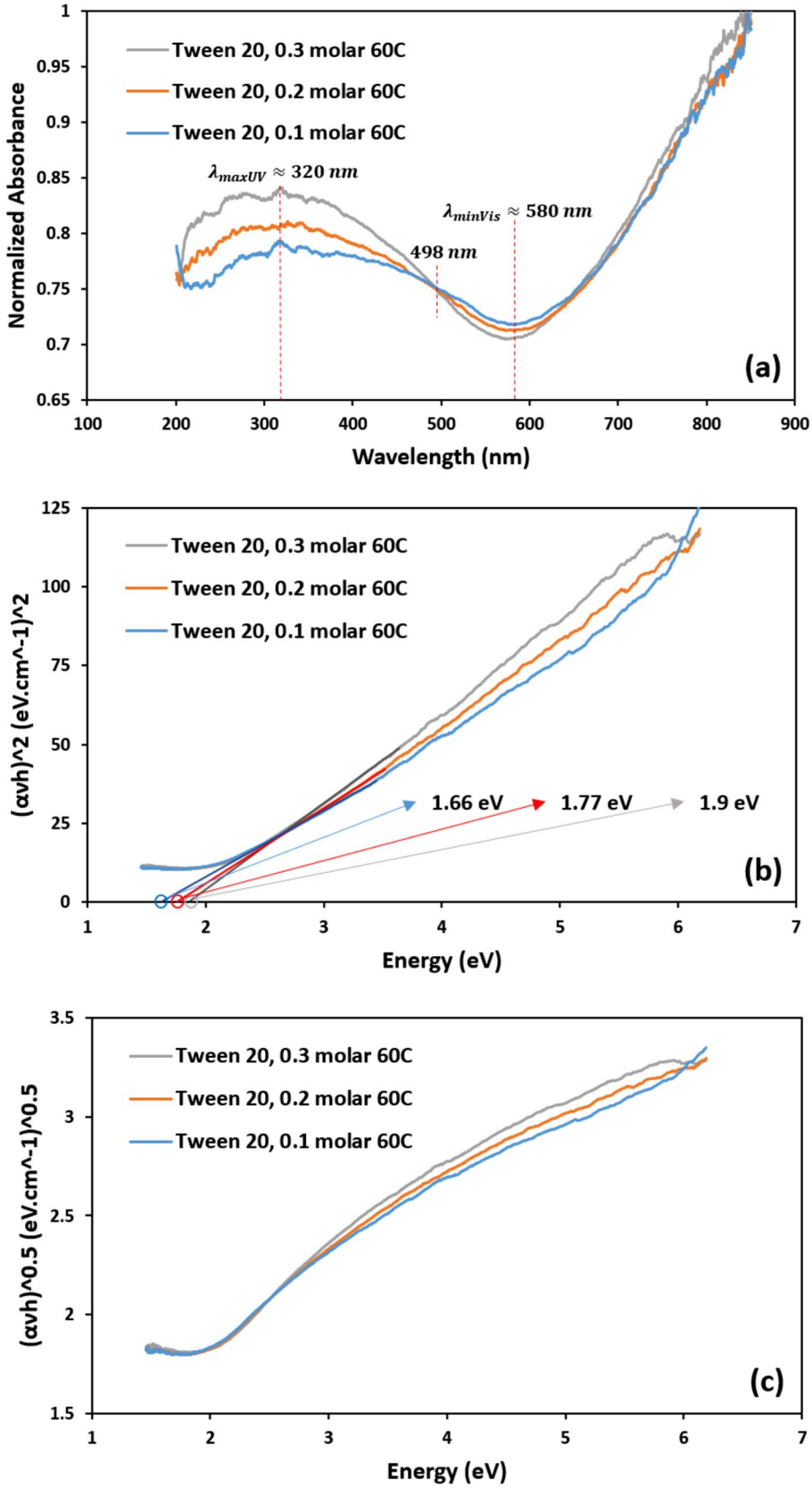

Fig. 5 **a** UV–Vis absorption graphs, **b** direct band gap Tauc plots and, **c** indirect band gap Tauc plots, for $Cu_{1.94}S$ nanoparticles synthesized with Tween 20 at 60 °C

method is expected to be at higher wavelengths than those obtained from UV–Vis absorption analysis, this value seems reasonable.

In addition, Fig. 6a shows the order of PL wavelength peaks as Tween 20, 0.1 molar > Tween 20, 0.2 molar > Tween 20, 0.3 molar which is in accordance with the order of band gap values depicted in Fig. 5b. It is also known that the better the crystallinity is obtained, the smaller the FWHM will be [55]. According to Fig. 6a, the order of FWHM values is Tween 20, 0.2 molar > Tween 20, 0.3 molar > Tween 20, 0.1 molar, which is consistent with the results of XRD analysis on crystallinity (Fig. 1a). The summary of UV–Vis and PL tests is presented in Fig. 6b. As illustrated in Fig. 6b, the electron excitation energy required for the transition from the valence band to the conduction band of $Cu_{1.94}S$ nanoparticles ranges from 1.66 to 1.9 eV. Then, through the path returning to valence band, they release a small amount of energy to reach the relaxation state. Then, they continue on their path to the valence band, releasing an energy of almost 1.56 eV. The return path is expected to experience a single relaxation state, a conclusion supported by the observation of a single peak in the PL test results (Fig. 6a). Another interesting point is the difference between the value of the bandgap and the PL released energy. This difference for $Cu_{1.94}S$ nanoparticles prepared with Tween 20 at 0.1, 0.2, and 0.3 molar concentrations is 0.1, 21, and 0.34 eV, respectively. The lower the difference, the fewer defects in crystallinity [56]. This finding demonstrates that $Cu_{1.94}S$ nanoparticles prepared with Tween 20 at 0.1 molar possess the lowest defects in their crystal structure.

3.4 LSV and EIS experiments

As illustrated in Fig. 7a, the schematic diagram provides a representation of the experimental cell utilized for the LSV and EIS tests. LSV plots of $Cu_{1.94}S$ electrodes versus bare titanium sheet are presented in Fig. 7b. The electrode related to $Cu_{1.94}S$ nanoparticles synthesized with 0.1 molar Tween 20 exhibited superior performance (with an onset potential of 650 mV and overpotentials of 685 mV at a current density of 20 mA/cm^2), while the bare titanium sheet (as depicted in the inset figure) demonstrated the lowest activity. Overall, all the electrodes prepared with $Cu_{1.94}S$ nanoparticles significantly enhanced the electrochemical activity of the bare titanium electrode. The Nyquist plots of $Cu_{1.94}S$ electrodes versus bare titanium electrode are given in Fig. 7c. All $Cu_{1.94}S$ electrodes showed a large reduction in charge transfer resistance compared to the bare titanium electrode. The measured charge transfer resistances for the prepared electrodes with $Cu_{1.94}S$ using 0.1 molar, 0.2 molar and 0.3 molar of Tween 20 are 0.227 kΩ, 0.744 kΩ, and 2.015 kΩ, respectively. Additionally, by comparing the Nyquist plots of the $Cu_{1.94}S$ electrodes, one can observe that increasing the mean particle size from 35 to 45 nm resulted in decreasing the charge transfer resistance from 2.015 kΩ to 0.227 kΩ.

4 Conclusions

This study demonstrated that spherical $Cu_{1.94}S$ nanoparticles synthesized via a low-temperature, atmospheric-pressure method exhibit promising photocatalytic activity under visible light. The use of Tween 20 as a capping agent was found to be essential for achieving the $Cu_{1.94}S$ phase, whereas Triton X-100 led to the formation of CuS. Notably, the synthesis was successfully conducted at 60 °C under ambient pressure, despite conventional requirements of temperatures above 80 °C and elevated pressures for the formation of $Cu_{1.94}S$. FESEM and TEM analyses revealed a strong tendency for the $Cu_{1.94}S$ nanoparticles to form aggregates. UV–Vis and PL measurements confirmed the direct band gap nature of $Cu_{1.94}S$. The band gap of $Cu_{1.94}S$ could be tuned from 1.9 to 1.66 eV by decreasing the Tween 20 concentration. Electrochemical evaluations using LSV and EIS in 1 M KOH demonstrated a marked enhancement in the performance of $Cu_{1.94}S$-coated electrodes compared to bare titanium. These findings highlight the potential of this facile and cost-effective synthesis method for further optimization and application of $Cu_{1.94}S$ nanoparticles in photocatalysis and photoelectrochemical systems, particularly with a focus on improving chemical and physical stability.

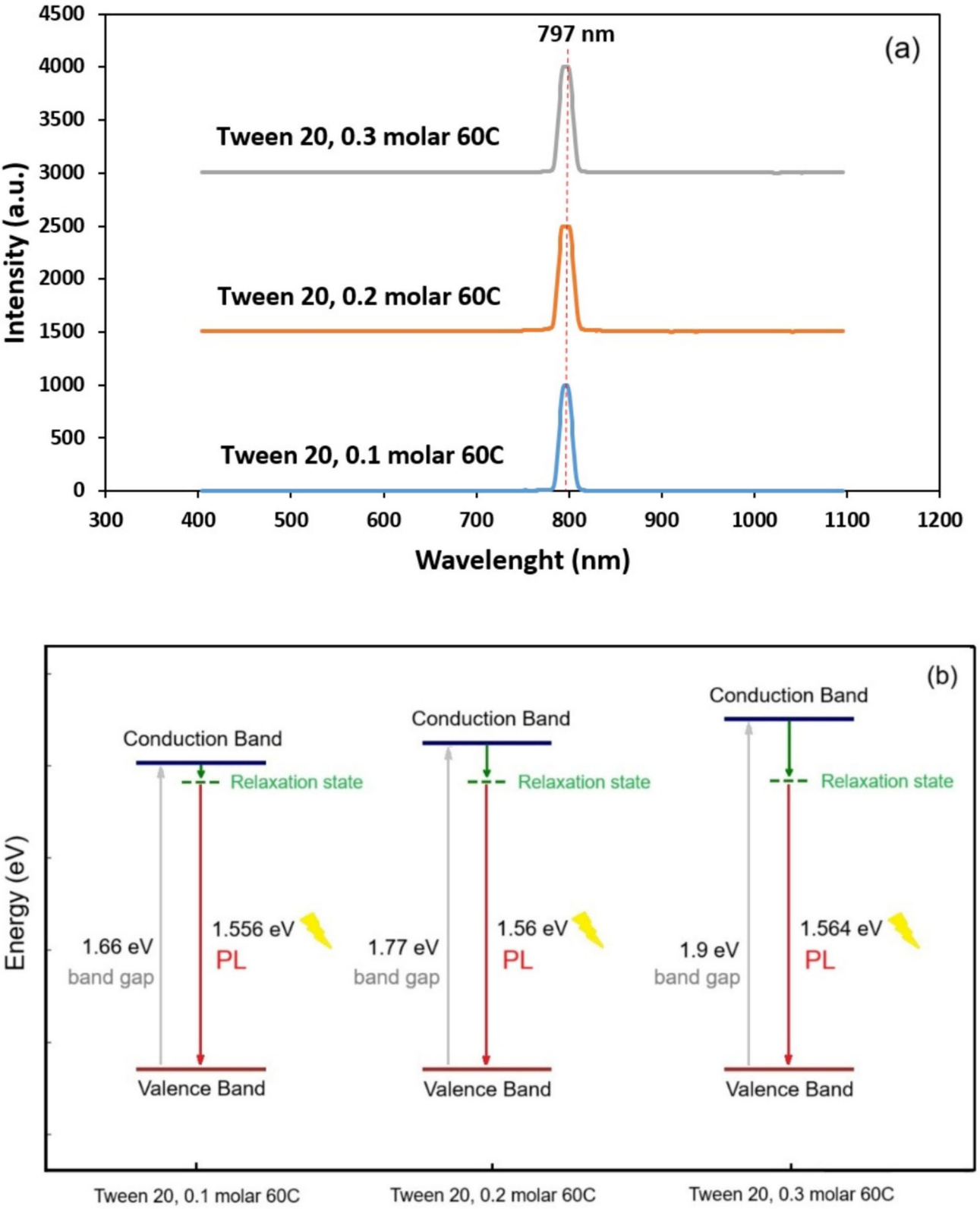

Fig. 6 **a** PL analysis results, and **b** band gap energy diagram, for the $Cu_{1.94}S$ nanoparticles synthesized with Tween 20 at 60 °C

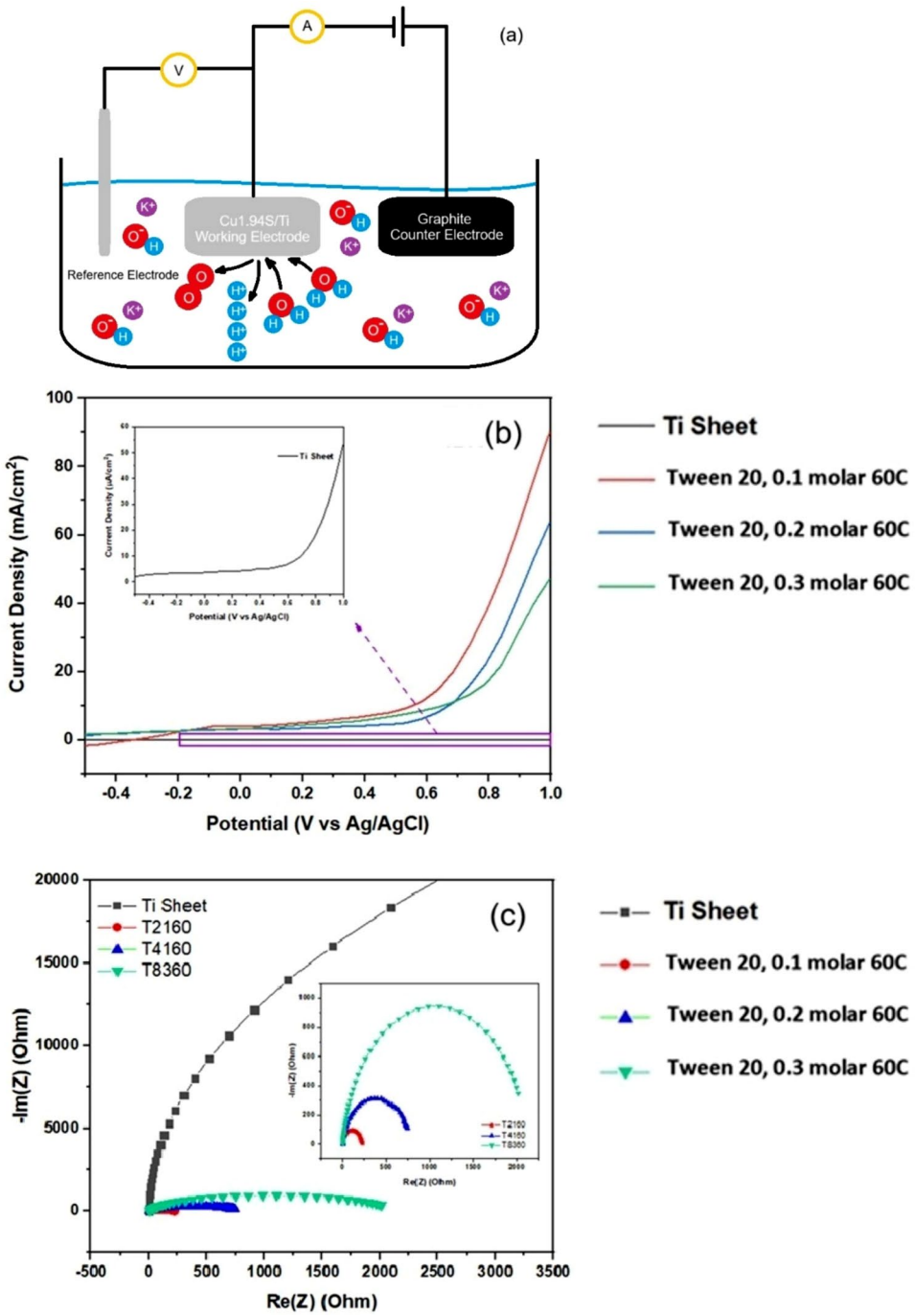

Fig. 7 Schemstic diagram of the experimental cell (**a**), LSV (**b**) and EIS (**c**) plots of the electrodes made with $Cu_{1.94}S$ nanoparticles synthesized with Tween 20 at 60 °C versus bare titanium electrode

Acknowledgements

We would like to extend our sincere gratitude to Khatam al-Anbia Air Defense University and Al-Hadba University for their continuous support and collaboration throughout the course of this study. Their guidance and contributions significantly shaped the direction of our research and were instrumental in helping us reach our objectives.

Author contributions

Farzad Namvar: data analysis, original draft writing, conceptualization and methodology. Seyed Ali

Hosseini Moradi: reviewing and editing, results discussion, investigation and supervision.

Funding

No financial support was received for the study.

Data availability

Data will be made available on request.

Declarations

Conflict of interest The author declares that there are no known competing financial interests or personal relationships that could appear to influence the work reported in this paper.

References

1. S.U. Rahayu, Y.-R. Wang, J.-B. Shi, M.-W. Lee, AgInS2/CdSe type-II core/shell quantum dot-sensitized solar cells with an efficiency of 11.75% under 0.1 sun. Sustain. Energy Fuels **8**, 113–124 (2024)
2. G. Du, Y. Ding, C. Li, L. Zhang, J. Li, M. Li, W. Zhu, C. He, Preparation of Cu/Cu2O/BC and its performance in adsorption-photocatalytic degradation of methyl orange in water. Materials **17**, 4306 (2024)
3. S.A.H. Moradi, Enhanced photocatalytic removal of tetracycline by ZnO/NiCo2O4 through the construction of a pn heterojunction. Chem. Phys. **587**, 112396 (2024)
4. P. Paredes, E. Rauwel, D.S. Wragg, L. Rapenne, E. Estephan, O. Volobujeva, P. Rauwel, Sunlight-driven photocatalytic degradation of methylene blue with facile one-step synthesized Cu-Cu2O-Cu3N nanoparticle mixtures. Nanomaterials **13**, 1311 (2023)
5. D. Hao, Y. Yang, B. Xu, Z. Cai, Bifunctional fabric with photothermal effect and photocatalysis for highly efficient clean water generation. ACS Sustain. Chem. Eng. **6**, 10789–10797 (2018)
6. L.M. Anaya-Esparza, E. Montalvo-González, N. González-Silva, M.D. Méndez-Robles, R. Romero-Toledo, E.M. Yahia, A. Pérez-Larios, Synthesis and characterization of TiO2-ZnO-MgO mixed oxide and their antibacterial activity. Materials **12**, 698 (2019)
7. D. Spanu, S. Recchia, S. Mohajernia, P. Schmuki, M. Altomare, Site-selective Pt dewetting on WO3-coated TiO2 nanotube arrays: an electron transfer cascade-based H2 evolution photocatalyst. Appl. Catal. B Environ. **237**, 198–205 (2018)
8. S. Chen, F. Liu, M. Xu, J. Yan, F. Zhang, W. Zhao, Z. Zhang, Z. Deng, J. Yun, R. Chen, First-principles calculations and experimental investigation on SnO2@ ZnO heterojunction photocatalyst with enhanced photocatalytic performance. J. Colloid Interface Sci. **553**, 613–621 (2019)
9. W. Avansi Jr., A.C. Catto, L.F. da Silva, T. Fiorido, S. Bernardini, V.R. Mastelaro, K. Aguir, R. Arenal, One-dimensional V2O5/TiO2 heterostructures for chemiresistive ozone sensors. ACS Appl. Nano Mater. **2**, 4756–4764 (2019)
10. A.M. Awan, A. Khalid, P. Ahmad, A.I. Alharthi, M. Farooq, A. Khan, M.U. Khandaker, S. Aldawood, M.A. Alotaibi, A.A. El-Mansi, Defects oriented hydrothermal synthesis of TiO2 and MnTiO2 nanoparticles as photocatalysts for wastewater treatment and antibacterial applications. Heliyon (2024). https://doi.org/10.1016/j.heliyon.2024.e25579
11. S.U. Din, S.H. Kiani, S. Haq, P. Ahmad, M.U. Khandaker, M.R.I. Faruque, A.M. Idris, M. Sayyed, Bio-synthesized tin oxide nanoparticles: structural, optical, and biological studies. Crystals **12**, 614 (2022)
12. A. Khalid, P. Ahmad, A.I. Alharth, S. Muhammad, M.U. Khandaker, M.R.I. Faruque, I.U. Din, M.A. Alotaibi, A practical method for incorporation of Fe (III) in Titania matrix for photocatalytic applications. Mater. Res. Express **8**, 045006 (2021)
13. S.A.H. Moradi, N. Ghobadi, F. Namvar, Influence of reduced graphene oxide loading on the structure, morphology and magnetic properties of Co0. 5Mn0. 3Cu0. 2Fe2O4 nanocomposites. J. Indian Chem. Soc. (2025). https://doi.org/10.1016/j.jics.2025.101868
14. F. Namvar, F. Beshkar, M. Salavati-Niasari, Novel microwave-assisted synthesis of leaf-like MnMoO4 nanostructures and investigation of their photocatalytic performance. J. Mater. Sci. Mater. Electron. **28**, 7962–7968 (2017)
15. S. Habib, F. Rashid, H. Tahir, I. Liaqat, A.A. Latif, S. Naseem, A. Khalid, N. Haider, U. Hani, R.A. Dawoud, Antibacterial and cytotoxic effects of biosynthesized zinc oxide and titanium dioxide nanoparticles. Microorganisms **11**, 1363 (2023)
16. A. Khalid, P. Ahmad, A.I. Alharthi, S. Muhammad, M.U. Khandaker, M. Rehman, M.R.I. Faruque, I.U. Din, M.A. Alotaibi, K. Alzimami, Structural, optical, and antibacterial efficacy of pure and zinc-doped copper oxide against pathogenic bacteria. Nanomaterials **11**, 451 (2021)

17. A. Khalid, P. Ahmad, A.I. Alharthi, S. Muhammad, M.U. Khandaker, M.R.I. Faruque, I.U. Din, M.A. Alotaibi, A. Khan, Synergistic effects of Cu-doped ZnO nanoantibiotic against Gram-positive bacterial strains. PLoS ONE **16**, e0251082 (2021)
18. A. Khalid, P. Ahmad, S. Muhammad, A. Khan, M.U. Khandaker, M.M. Alam, M. Asim, I.U. Din, J. Iqbal, I.U. Rehman, Synthesis of boron-doped zinc oxide nanosheets by using *phyllanthus emblica* leaf extract: a sustainable environmental applications. Front. Chem. **10**, 930620 (2022)
19. S.A.H. Moradi, D.A. Oleiwi, K. Heydaryan, S.H. Abed, F. Namvar, UV-responsive Er-doped NiAl2O4/Mn/GO nanocomposites: green synthesis and photocatalytic degradation of organic pollutants via fluorescent behavior for water purification. J. Fluoresc. (2025). https://doi.org/10.1007/s10895-025-04357-0
20. F. Namvar, F. Beshkar, M. Salavati-Niasari, S. Bagheri, Morphology-controlled synthesis, characterization and photocatalytic property of hierarchical flower-like Dy2Mo3O9 nanostructures. J. Mater. Sci. Mater. Electron. **28**, 10313–10320 (2017)
21. S.A. Ali, S.M. Alshehri, T. Ahmad, Rational integration of MoSe2 and BN with TiO2 to design nanoengineered ternary heterojunctions for sustainable hydrogen energy: experimental evidences and theoretical anticipations. Int. J. Hydrogen Energy **82**, 1182–1195 (2024)
22. S.A. Ali, S. Majumdar, P.K. Chowdhury, S.M. Alshehri, T. Ahmad, Ultrafast charge transfer dynamics in multifaceted quaternary Te–MoTe2–MoS2/ZnO S-scheme heterostructured nanocatalysts for efficient green hydrogen energy. ACS Appl. Energy Mater. **7**, 7325–7337 (2024)
23. R. Gupta, S.A. Ali, T. Upma, R.G. Ahmad, Unprecedented hydrogen evolution reactions based on the accelerating effect of [Co–Tb]-supramolecular complex-anchored CdS heterojunctions. ACS Appl. Mater. Interfaces **17**, 28244–28255 (2025)
24. A. Mehtab, P.P. Ingole, J. Ahmed, Y. Mao, T. Ahmad, Unraveling quantum mysteries: probing the interplay of CdS quantum dots and g-C3N4 nanosheets for enhanced photo/electrocatalytic hydrogen evolution. J. Phys. Chem. C Nanomater. Interfaces. **128**, 85–94 (2023)
25. M. Khani, S.E. Mousavi, H. Pahlavanzadeh, H. Ale Ebrahim, A. Mozaffari, Study of MoO 3-γAl 2 O 3 catalysts behavior in selective catalytic reduction of SO 2 toxic gas to sulfur with CH 4. Environ. Sci. Pollut. Res. **26**, 9686–9696 (2019)
26. A. Sudhaik, P. Raizada, S. Rangabhashiyam, A. Singh, V.-H. Nguyen, Q.V. Le, A.A.P. Khan, C. Hu, C.-W. Huang, T. Ahamad, Copper sulfides based photocatalysts for degradation of environmental pollution hazards: a review on the recent catalyst design concepts and future perspectives. Surf. Interface Anal. **33**, 102182 (2022)
27. P. Lukashev, W.R. Lambrecht, T. Kotani, M. Van Schilfgaarde, Electronic and crystal structure of Cu_2−xS: full-potential electronic structure calculations. Phys. Rev. B Condens. Matter Mater. Phys. **76**, 195202 (2007)
28. A.B. Martinson, S.C. Riha, E. Thimsen, J.W. Elam, M.J. Pellin, Structural, optical, and electronic stability of copper sulfide thin films grown by atomic layer deposition. Energy Environ. Sci. **6**, 1868–1878 (2013)
29. M.S. Sadek, G.E. Khedr, M.F.A. Messih, M.A.H. Ismail, Experimental and DFT study of photocatalytic activity of reduced graphene oxide/copper sulfide composite for removal of organic dyes from water. Sci. Rep. **13**, 15636 (2023)
30. H. Yawei, F. Tong, R. Miao, Z. Yan, Z. Ning, Preparation and enhanced photocatalytic properties of Cu31S16/Cu9S5 heterojunction composite. J. Sulfur Chem. **45**, 239–249 (2024)
31. A. Enesca, L. Isac, Photocatalytic activity of cu2s/wo3 and cu2s/sno2 heterostructures for indoor air treatment. Materials **14**, 3656 (2021)
32. M. Patel, K.K. Joshi, K.H. Modi, P.M. Pataniya, S. Siraj, P. Sahatiya, C. Sumesh, CuS nanoparticles: an efficient electrocatalyst for hydrogen evolution reaction in a wide pH range. Electrochim. Acta **441**, 141740 (2023)
33. M. Yusuf, S.A. Hira, K.H. Park, Light-harvesting novel hierarchical porous Cu9S5–MnWO4 hybrid structures in photocatalytic oxidative homocoupling of alkynes and amines. ACS Appl. Mater. Interfaces **14**, 15529–15540 (2022)
34. B. Van Thang, H.T. Tung, D.H. Phuc, T.P. Nguyen, T. Van Man, L.Q. Vinh, High-efficiency quantum dot sensitized solar cells based on flexible rGO-Cu2S electrodes compared with PbS, CuS, Cu2S CEs. Sol. Energy Mater. Sol. Cells **250**, 112042 (2023)
35. Z. Guo, X. Ming, G. Wang, B. Hou, X. Liu, T. Mei, J. Li, J. Wang, X. Wang, Super-hydrophilic copper sulfide films as light absorbers for efficient solar steam generation under one sun illumination. Semicond. Sci. Technol. **33**, 025008 (2018)
36. S.-W. Gu, Y.-X. Zhang, J. Guo, J. Feng, Z.-H. Ge, Effects of sintering temperature on thermoelectric properties of Cu1.8S bulk materials. Mater. Res. Express **7**, 015923 (2020)
37. A. Narjis, A. Outzourhit, A. Aberkouks, M. El Hasnaoui, L. Nkhaili, Structural and thermoelectric properties of copper sulphide powders. J. Semicond. **39**, 122001 (2018)

38. K. Okamoto, S. Kawai, Electrical conduction and phase transition of copper sulfides. Jpn. J. Appl. Phys. **12**, 1130 (1973)
39. M. Li, Y. Liu, Y. Zhang, X. Han, T. Zhang, Y. Zuo, C. Xie, K. Xiao, J. Arbiol, J. Llorca, Effect of the annealing atmosphere on crystal phase and thermoelectric properties of copper sulfide. ACS Nano **15**, 4967–4978 (2021)
40. X. Zuo, X. Han, Y. Lu, Y. Liu, Z. Wang, J. Li, K. Cai, Largely enhanced thermoelectric power factor of flexible Cu2− xS film by doping Mn. Materials **16**, 7159 (2023)
41. S. Iqbal, A. Bahadur, S. Anwer, S. Ali, A. Saeed, R.M. Irfan, H. Li, M. Javed, M. Raheel, M. Shoaib, Shape and phase-controlled synthesis of specially designed 2D morphologies of l-cysteine surface capped covellite (CuS) and chalcocite (Cu2S) with excellent photocatalytic properties in the visible spectrum. Appl. Surf. Sci. **526**, 146691 (2020)
42. D. Li, J. Ma, L. Zhou, Y. Li, C. Zou, Synthesis and characterization of Cu2S nanoparticles by diethylenetriamine-assisted hydrothermal method. Optik **126**, 4971–4973 (2015)
43. C.-Y. Chen, J.-R. Jiang, W.-S. Chuang, M.-S. Liu, S.-W. Lee, Development of crystalline Cu2S nanowires via a direct synthesis process and its potential applications. Nanomaterials **10**, 399 (2020)
44. L.A. Saona, J.L. Campo-Giraldo, G. Anziani-Ostuni, N. Órdenes-Aenishanslins, F.A. Venegas, M.F. Giordana, C. Díaz, M. Isaacs, D. Bravo, J.M. Pérez-Donoso, Cysteine-mediated green synthesis of copper sulphide nanoparticles: biocompatibility studies and characterization as counter electrodes. Nanomaterials **12**, 3194 (2022)
45. H. Pathan, J. Desai, C. Lokhande, Modified chemical deposition and physico-chemical properties of copper sulphide (Cu2S) thin films. Appl. Surf. Sci. **202**, 47–56 (2002)
46. K. Zhuo, J. Wang, J. Gao, U. Landman, M.-Y. Chou, Liquidlike Cu atom diffusion in weakly ionic compounds Cu 2 S and Cu 2 Se. Phys. Rev. B **102**, 064201 (2020)
47. C. Ma, L. Zhu, X. Qiao, H. Li, X. Zhu, J. Xue, Q. Xue, Ni-doped brochantite@ copper hydroxide hierarchical structures on copper mesh with ultrahigh oil-resistance for high-efficiency oil/water separation. Surf. Coat. Technol. **406**, 126642 (2021)
48. M.P. Ravele, O.A. Oyewo, D.C. Onwudiwe, Controlled synthesis of CuS and Cu9S5 and their application in the photocatalytic mineralization of tetracycline. Catalysts **11**, 899 (2021)
49. Z.H. Li, K.O. Egbo, X.H. Lv, Y. Wang, K.M. Yu, C.P. Liu, Electronic structure and properties of Cu2-xS thin films: dependence of phase structures and free-hole concentrations. Appl. Surf. Sci. **572**, 151530 (2022)
50. D. Zhu, A. Tang, H. Ye, M. Wang, C. Yang, F. Teng, Tunable near-infrared localized surface plasmon resonances of djurleite nanocrystals: effects of size, shape, surface-ligands and oxygen exposure time. J. Mater. Chem. C **3**, 6686–6691 (2015)
51. K. Nemade, S. Waghuley, Band gap engineering of CuS nanoparticles for artificial photosynthesis. Mater. Sci. Semicond. Process. **39**, 781–785 (2015)
52. D. Zhu, H. Ye, Z. Liu, J. Liu, H. Fu, Y. Huang, F. Teng, Z. Wang, A. Tang, Seed-mediated growth of heterostructured Cu 1.94 S-MS (M = Zn, Cd, Mn) and alloyed CuNS 2 (N = In, Ga) nanocrystals for use in structure-and composition-dependent photocatalytic hydrogen evolution. Nanoscale **12**, 6111–6120 (2020)
53. A.L. Abdelhady, K. Ramasamy, M.A. Malik, P. O'Brien, S.J. Haigh, J. Raftery, New routes to copper sulfide nanostructures and thin films. J. Mater. Chem. **21**, 17888–17895 (2011)
54. K. Nemade, S. Waghuley, Low temperature synthesis of semiconducting α-Al2O3 quantum dots. Ceram. Int. **40**, 6109–6113 (2014)
55. M. Bellardita, A. Di Paola, B. Megna, L. Palmisano, Determination of the crystallinity of TiO2 photocatalysts. J. Photochem. Photobiol. A, Chem. **367**, 312–320 (2018)
56. X. Guo, S. Liu, W. Wang, C. Li, Y. Yang, Q. Tian, Y. Liu, Plasmon-induced ultrafast charge transfer in single-particulate Cu 1.94 S-ZnS nanoheterostructures. Nanoscale Adv. **3**, 3481–3490 (2021)